



Mechanical property evaluation of 3D multi-phase cement paste microstructures reconstructed using generative adversarial networks

Sung-Wook Hong^a, Se-Yun Kim^a, Kyoungsoo Park^a, Kenjiro Terada^b, Hoonhee Lee^c, Tong-Seok Han^{a,*}

^a Department of Civil and Environmental Engineering, Yonsei University, Seoul 03722, Republic of Korea

^b International Research Institute of Disaster Science, Tohoku University, Sendai 980-8572, Japan

^c Halla Cement Corp., Gangneung, Gangwon 25645, Republic of Korea

ARTICLE INFO

Keywords:

Cement paste
Microstructure
Generative adversarial networks
Mechanical properties
Phase-field fracture model
Micro-CT

ABSTRACT

This study proposes an artificial intelligence based framework for reconstructing the 3D multi-phase cement paste microstructure to evaluate its mechanical properties using simulation. The reconstruction of cement paste microstructures is performed using modified generative adversarial networks (GANs) based on microstructural images from micro-CT. For computational efficiency, 2D microstructures are first reconstructed and then extended to 3D microstructures. The reconstructed microstructures exhibit the same microstructural features as the original microstructures when characterized by probability functions. Mechanical properties such as stiffness and tensile strength are evaluated for the original and reconstructed specimens using a phase-field fracture model, and similar behaviors are observed. The results confirm that the reconstructed virtual microstructures can be used to supplement the real microstructures in evaluating the mechanical properties of 3D multi-phase cement paste. This approach thus provides a critical element of a data-driven approach to correlating its microstructure and properties.

1. Introduction

Property evaluation of cementitious materials through experiments is time and effort-intensive. Simulating material properties that can supplement the experimental results can accelerate the analysis of new and existing material behaviors. However, due to the complex microstructural features of cementitious materials, including cement paste, reconstructing virtual specimens that share similar microstructural characteristics is challenging. More recently, advances in artificial intelligence approaches have enabled the reconstruction of complex microstructures. Among the approaches, generative adversarial networks (GAN) [1–5] are found to be effective for such a task. This study proposes a computationally efficient framework for reconstructing multi-phase cement paste microstructures from micro-CT and analyzes the mechanical properties evaluated from the reconstructed microstructures.

The reconstruction of microstructures with complex features has been investigated and is used for evaluating properties through virtual experiments. Random heterogeneous materials characterized by low-order probability functions were successfully reconstructed using stochastic optimization techniques [6–10]. The method was also applied to reconstruct cementitious materials, and the reconstructed

microstructures were used to evaluate the permeability of porous concrete [11] and cement paste [12], the stiffness and thermal conductivity of the interfacial transition zone (ITZ) [13], and to perform a sensitivity analysis of the stiffness and strength of cement paste [14]. Although microstructures reconstructed using stochastic optimization were effective for property evaluation of cementitious materials, the reconstructed microstructures were limited to two phases (pore and solid) owing to computational cost. For a more accurate analysis of localized behaviors such as strength, a more detailed microstructural model as proposed in Refs. [15–21] is preferable. In these studies, cement paste microstructures were modeled as multiple solid phases, and simulations were performed to demonstrate that cracks propagated through the weak solid phase. In particular, Refs. [15–18] and relevant works modeled the multi-phase cement paste incorporating uncertainties based on micro-CT images, and evaluated its properties using the lattice model. However, the reconstruction of an accurate multiple solid phase microstructure using the conventional stochastic optimization method for continuum based simulations requires significant effort; therefore, alternative approaches are recommended for efficiency.

* Corresponding author.

E-mail address: tshan@yonsei.ac.kr (T.-S. Han).

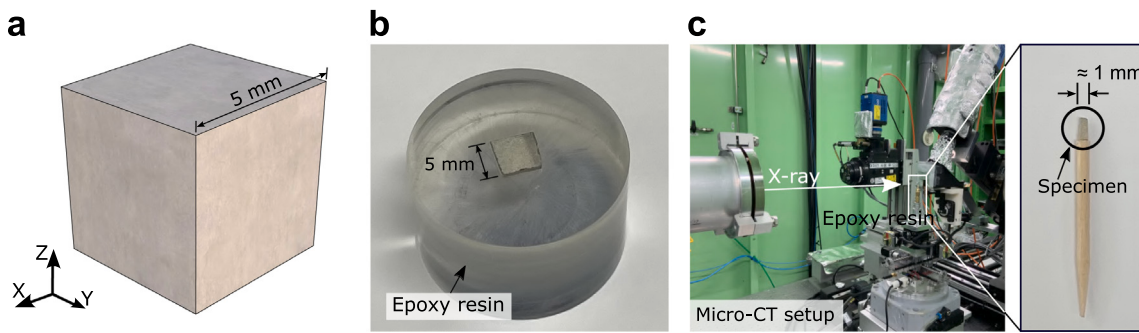


Fig. 1. Cement paste specimens. (a) Cubic specimen, (b) Nanoindentation specimen, (c) Micro-CT specimen.

As deep learning techniques are widely available, the reconstruction of complex three-dimensional (3D) microstructures from two-dimensional (2D) or 3D microstructural information becomes, and extensive articles have been recently published. For example, 2D to 3D microstructure reconstruction approaches using transfer learning [22, 23] and stochastic optimization with gradient-based or machine learning [24,25] were proposed. Microstructure reconstruction using a generative adversarial network (GAN) model can be found including 2D to 3D microstructure reconstruction techniques [26–28]. The deep-learning approach was also applied for reconstructing cementitious materials and geomaterials. In Ref. [29], 2D concrete three-phase (pore, binder, and aggregate) microstructures were generated using GAN from micro-CT images, and the mechanical properties were estimated. The characteristics of cement paste microstructures were investigated using deep learning to obtain insights into microstructure reconstruction [30]. Three-dimensional two-phase porous media microstructures were characterized and reconstructed using an efficient GAN [31]. Three-dimensional shale and beadpack two-phase (pore and solid) microstructures were reconstructed using a multiscale GAN [32]. Additionally, a cellular automata approach controlled by deep learning networks for reconstructing hydrating 3D multi-phase cement paste microstructures was proposed in Ref. [33].

Among the deep learning models, variational autoencoder (VAE) [34–36], diffusion model [37–39], and the GAN model have been used to reconstruct microstructures with complex geometries. The VAE model is relatively easy to train and diverse features can be reconstructed. However, the VAE model often suffers from low fidelity and blurred microstructural features in reconstructed samples. The diffusion model reconstructs high-fidelity samples with diverse features, but it tends to generate samples slowly because it requires multiple passes through the neural network compared with the VAE and GAN models. In addition, the diffusion model is more complex to implement and requires a higher computational cost than the other models. Although the GAN model is relatively difficult to train because of the two loss functions (generator and discriminator), the model can generate high-fidelity samples with a desired level of diversity. In this study, we propose an extended GAN method to reconstruct 3D four-phase cement paste microstructures consisting of pore, outer product, inner product, and unhydrated phases to validate the method by comparing the microstructural characteristics and mechanical properties (stiffness and tensile strength) of the original and reconstructed specimens.

The original microstructures of cement paste can be obtained nondestructively using micro-CT. The micro-CT has been successfully used to investigate the microstructural features of cement paste and its correlation to material properties [40–43]. The micro-CT-based cement paste images are characterized as multi-phase microstructures, and their properties are evaluated using simulation tools such as lattice models (e.g., Refs. [15–18,44]) and continuum-based models (e.g., Refs. [19, 45–48]). In particular, a framework to evaluate the mechanical properties of cement paste using a phase-field fracture model [49,50], an extension of a continuum damage model, is proposed in Ref. [19] with

multi-phase microstructures obtained from synchrotron X-ray micro-CT and nanoindentation test results. In Ref. [19], the differences in mechanical responses between multi-phase and homogenized models were compared. It is confirmed that the multi-phase solid model can capture the realistic crack propagation patterns observed from the experiments in Ref. [21]. In this study, a method for reconstructing virtual multiple-solid-phase microstructures is investigated. The characteristics and mechanical properties of the reconstructed specimens are compared with those of the original microstructures to confirm that the reconstructed microstructures can supplement the microstructures obtained from the micro-CT measurements.

In the next section, materials for the analysis are described. Then, methods for investigating microstructural characteristics, performance evaluation tools, and deep learning techniques are briefly presented. The procedure for reconstructing cement paste microstructures is described next, followed by the mechanical performance evaluation and analysis section. Finally, further works are discussed, and conclusions are summarized.

2. Materials and methods

2.1. Specimens

The cement paste specimens were prepared using ordinary Portland cement with a water/cement ratio (w/c) of 0.4. The specimens were cast in cubic $5 \times 5 \times 5 \text{ mm}^3$ silicon molds and were demolded after 24 h (Fig. 1a). The specimens were cured in water at room temperature for 28 days. The samples were then submerged in isopropanol to prevent further hydration. A specimen for the nanoindentation test is presented in Fig. 1b. The 5 mm cubic specimen was sliced, impregnated with epoxy resin in a vacuum chamber to remove pores and prevent damage, and cured for 8 h, followed by grinding and polishing. Specimens for obtaining high-resolution microstructures from micro-CT scans are prepared by carefully breaking each specimen to a width of 1 mm (Fig. 1c) shortly before measurements. The shape of the specimens for CT measurements was irregular, but the largest width of the cross section in the direction of the X-ray was approximately 1 mm. The specimen height did not affect the X-ray CT image quality; therefore, it was not reduced to be comparable with the cross-sectional width, but was maintained large enough to handle the specimen conveniently. The specimen preparation procedure used in Refs. [20,21,51] was used. More details can be found in the references.

2.2. Nanoindentation

The nanoindentation test with Berkovich tip was conducted for identifying the input modeling parameters of the cement paste microstructure. The load control was used to conduct the test (a maximum load: 20 mN). The loading time was 20 s, held for 2 s at the maximum load, and unloaded for 20 s. Indentation probes were conducted on a 10×10 grid with $20 \mu\text{m}$ spacing, so the measurement domain was

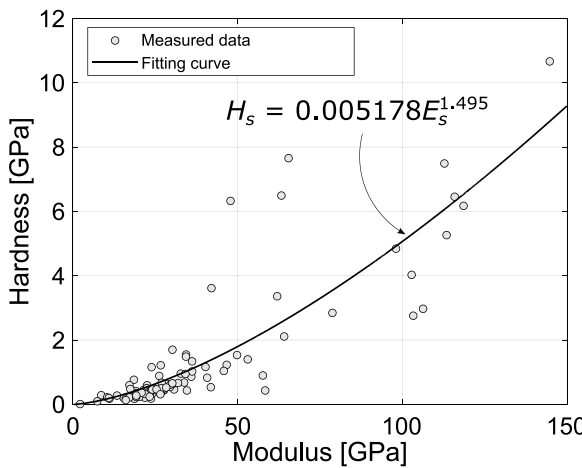


Fig. 2. Correlation between Young's modulus (E_s) and hardness (H_s) for solid phases from nanoindentation results.

$180 \times 180 \mu\text{m}^2$. The 100 indentation points were confirmed to be sufficient for phase distribution characterization and input material modeling parameter identification for cement paste microstructures with four phases, which are pore and three solid phases (outer, inner product, and unhydrated phases) [19,20,52]. From the indentation test, Young's modulus distribution and the correlation between Young's modulus (E_s) and hardness (H_s) (Fig. 2) of the solid phases are obtained and used to identify the material parameters combined with the characteristics of micro-CT images.

2.3. Micro-CT

The three dimensional cement paste microstructures with a voxel size of $0.65 \mu\text{m}$ were obtained from specimens less than 1 mm wide using a synchrotron X-ray micro-CT (energy level: 25 keV) at Pohang Accelerator Laboratory in the Republic of Korea (Fig. 3a). Each voxel is assigned a grayscale value in image format (Fig. 3b). The value can be linearly transformed to linear attenuation coefficient (LAC), which can be considered as a material characteristic [53]. The distribution of grayscale or LAC value (χ) in correlation with nanoindentation results is used to determine the threshold values for phase segmentation. The LAC value is normalized ($\bar{\chi}$) so that the pore threshold is assigned to 0, and the peak LAC of unhydrated phase is set to 1 [20].

2.4. Lineal-path function

In this study, microstructural features are characterized by the lineal-path (L) function [10] (Fig. 4), which is used to characterize

cement paste microstructure. The lineal-path function was found to be effective for identifying phase characteristics, such as continuity, of random heterogeneous materials, including cement paste, and for confirming the similarity or statistical identity of the microstructures [51, 54–58]. In a domain with side length D , the lineal-path function $L_\alpha(r)$ is a probability of placing a line of length r entirely within a phase α . Phase α can be one of the four phases for the cement paste microstructure. However, the evaluation of the multi-phase cement paste microstructures obtained from micro-CT using simulations confirmed that the weaker hydrated phase and pore microstructural features dominated the material strength (e.g., Refs. [16–18]). It was also demonstrated that simulated cracks tend to propagate through the weaker hydrated phase (outer product), and this prediction was validated experimentally [20,21,51]. Therefore, the pore (p) and outer product (o) phases were characterized because they were the most influential phases contributing to the mechanical behavior, considering their phase volume fraction and strength.

Phase continuity is further characterized by the parameter ℓ_{La} [20]. For a random heterogeneous material, an exponential function can be used to approximate the lineal-path function $L_\alpha(r)$ for phase α as

$$L_\alpha(r) = \phi_\alpha \exp\left(-\frac{r}{\ell_{La}}\right), \quad (1)$$

where ϕ_α is the phase volume fraction and r is the line length. By definition, ℓ_{La} is the intersection between the initial slope of $L_\alpha(r)$ and the r axis, which is shown in Fig. 4. The parameter ℓ_{La} can serve as a characteristic scalar parameter for representing $L_\alpha(r)$.

2.5. Phase-field fracture model

The phase-field fracture model is used to conduct direct tension tests to obtain the mechanical behaviors of the cement paste microstructures. The phase-field fracture model, and extension of the damage model, adopted and implemented for this study is based on the formulation presented in Refs. [49,50], and only a short summary is described here. A damage variable d for the phase-field diffusive crack ranges from 0 (no crack) to 1 (complete crack) at each material point. Four parameters are required for the model as input parameters for solid phases [20]. The Young's modulus E_s and Poisson's ratio (ν) are related to elasticity, and the peak tensile strength (σ_s) and diffusive crack width (l) are related to fracture. E_s and σ_s are determined from the nanoindentation results and grayscale level (or LAC) of the micro-CT images as in Refs. [20,51]. The value of 0.2 is assumed for the Poisson's ratio ν , and twice the element size ($2h$) is selected for the diffusive crack width l , the minimum value required for the model [49]. More details on efficient and effective modeling can be found in Refs. [20,21]. The simulation procedure is described further in Section 4.1.

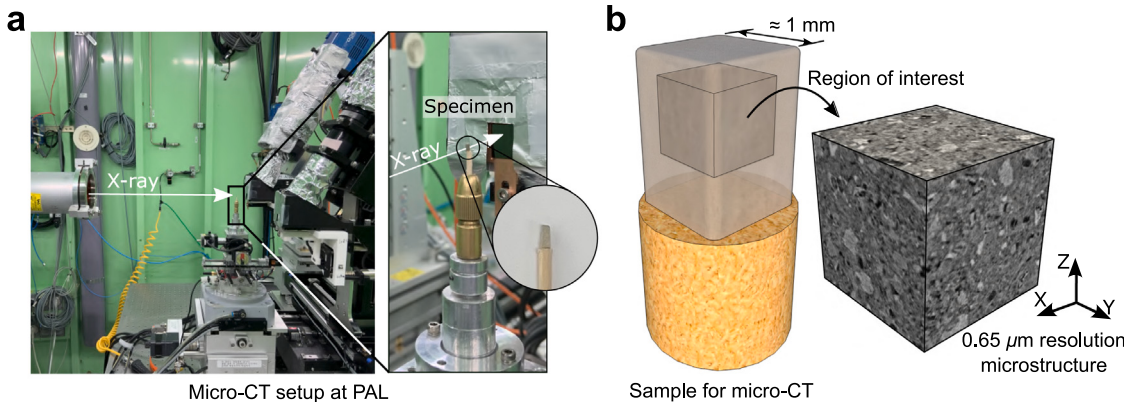


Fig. 3. Micro-CT setup and sample microstructure. (a) Micro-CT device at the Pohang Accelerator Laboratory (PAL), (b) Cement paste microstructure with $0.65 \mu\text{m}$ resolution.

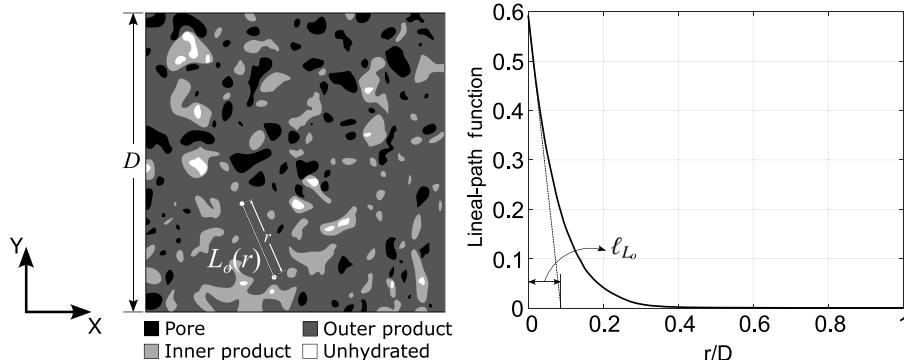


Fig. 4. Example of microstructure consisting of four phases, and its lineal-path function $L_o(r)$ and parameter ℓ_{L_o} for the outer product.

2.6. Generative adversarial network (GAN)

The generative adversarial network (GAN) [1] is a framework for estimating generative models using the adversarial process. In the framework, two models are trained. One model, generator G , generates or reconstructs data based on characteristics from the original samples. The other model, discriminator D , estimates the probability that the data is from the original samples. The two models are trained through an adversarial process by the interactions between the two models, through which the characteristics of the generated data sets become similar to those of the original samples. Enhanced from the general GAN, cycle generative adversarial networks (CycleGAN) [2] were proposed to reconstruct images more accurately. A summary of the algorithm of CycleGAN is presented in Appendix A. The CycleGAN algorithm was adopted with modified networks specific to this current study. The network used for reconstructing 3D cement paste microstructures from 2D cement paste images is described in detail in the next section.

3. Microstructure reconstruction

The cement paste microstructure reconstruction process using the extended CycleGAN is presented. First, the procedure to obtain the target microstructures is described. Then, the reconstruction procedure using CycleGAN [2] and extensions proposed in this study are followed. The deep learning-based reconstruction process was implemented as an extension of TensorFlow [59], and the related terms are consistent with those used in TensorFlow.

3.1. Target microstructure

The target microstructures for reconstruction were segmented into four phases from the original micro-CT images following the procedure and the data presented in Ref. [21]. First, to segment the cement paste microstructure, Young's modulus distribution obtained from nanoindentation is fitted by three superposed Gaussian curves (Fig. 5a). The intersection between the first and second Gaussian curves from the left was used as the outer and inner product phase thresholds. Likewise, the intersection between the second and third Gaussian curves determined the threshold value to distinguish the inner product from the unhydrated phases. Then, from the linear attenuation coefficient (LAC, χ) distribution from the original micro-CT microstructure (Fig. 5b), the threshold value to segment pores from the solid phases is selected by the intersection between the tangents from the maximum points of the first and second derivatives. The threshold between the unhydrated and other solid phases was determined by locating the intersection between the two right-most Gaussian curves after approximating the LAC distribution using four Gaussian curves. The threshold to separate the outer product from the inner product was determined from volume ratio of the outer to inner products from nanoindentation. An example

of an original cement paste microstructure from micro-CT shown in Fig. 5c can then be segmented to a four-phase target microstructure shown in Fig. 5d.

The side length of the microstructure was 83.2 μm with the voxel size of 0.65 μm , so $128 \times 128 \times 128$ voxels constitute each microstructure. The side length of 83.2 μm for a cement paste microstructure should be large enough to evaluate its mechanical properties at the microscale based on previous studies [17,19,55]. The representative volume element (RVE) as a binder in concrete could be actually much larger depending on the additional microstructural features (e.g., void clusters) or even may not exist because of the localized behavior of cementitious materials [60]. However, the microstructure size was found to be adequate when comparing the property evaluation between the target and reconstructed microstructures.

3.2. Reconstructed microstructure

3.2.1. Adapted CycleGAN

An extension of the general GAN, CycleGAN [2], is used to reconstruct the cement paste microstructure. We adapted the network to our framework for microstructure reconstruction. The direct connections of the autoencoder for convolutional neural networks (CNNs) proposed in Ref. [5] were adopted for an effective outcome. A more detailed description of the adapted network can be found in Appendix B. CNNs [61] were trained with data through the gradient descent method. The network is schematically presented in Fig. 6.

GAN model for training and reconstructing 3D microstructures requires a significant amount of parameters, resulting in huge computational costs. Thus, in this study, a two-step process is proposed. The first step is a 2D microstructure reconstruction process, and the second step is a 2D to 3D microstructure reconstruction process. The 2D generator produces a “fake” 2D microstructure from a noise image as an input (Fig. 6). The noise image comprises randomly distributed pixel-based four phases with volume fractions obtained from a target microstructure. The “real” images are taken from 2D sections of the 3D micro-CT microstructures. The “fake” and “real” 2D microstructural images are provided to the discriminator. The generator and discriminator networks are both composed of CNNs. In particular, the discriminator utilizes PatchGAN [62]. For an effective reconstruction process, the direct connections between the encoder and decoder in the autoencoder of 2D and 3D generators are used. Encoder information is “concatenated” to the decoder information to incorporate previously missing features during the transposed convolution process.

The number of 2D images used for the training and test processes was 491,500 and 500, respectively. For the training dataset of the 3D microstructures, 60 microstructures were augmented to 3200 microstructures through image rotation and reflection. The similarity of target and reconstructed specimens of both 2D and 3D microstructures during the training process (Fig. 6) were confirmed by comparing the phase volume fractions and phase continuity (ℓ_L and Eq. (1)) of the

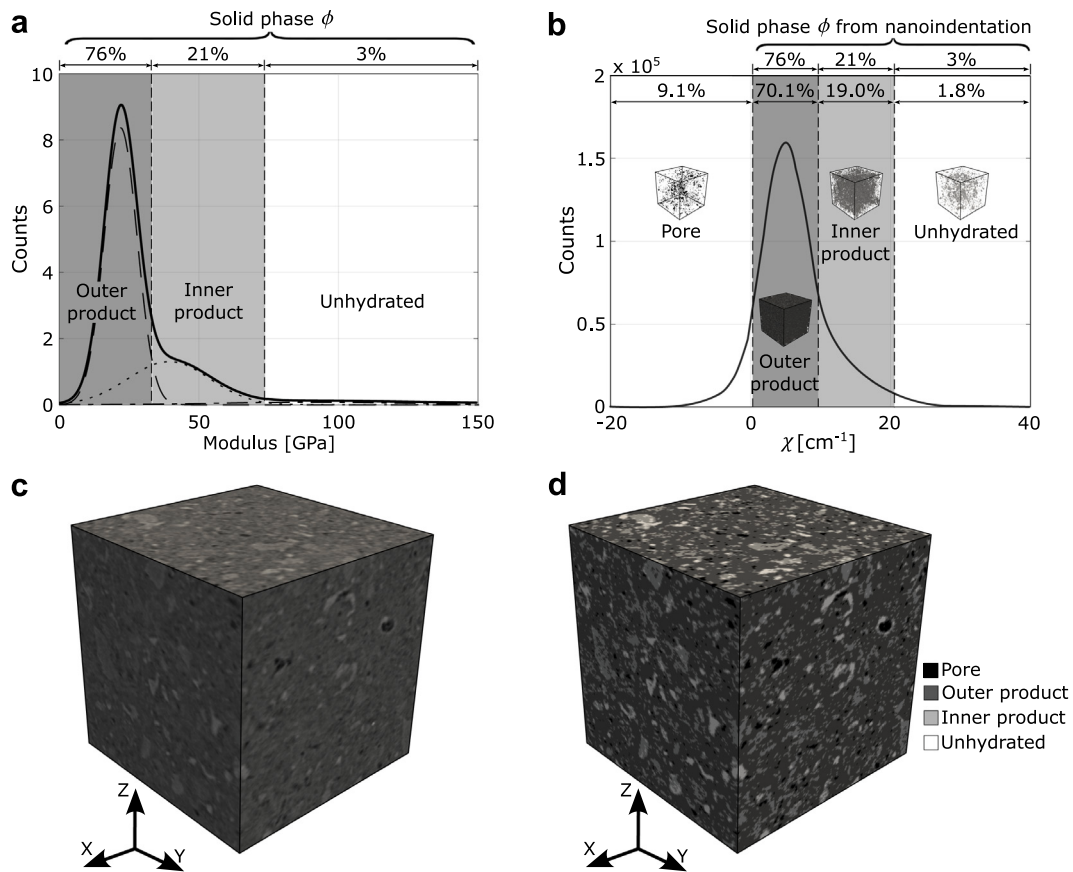


Fig. 5. Cement paste microstructure phase segmentation. (a) Young's modulus (E) distribution from nanoindentation, (b) Linear attenuation coefficient (LAC, χ) distribution from micro-CT, (c) Original microstructure from micro-CT (8-bit grayscale image), (d) Segmented four-phase microstructure. (ϕ : volume fraction)

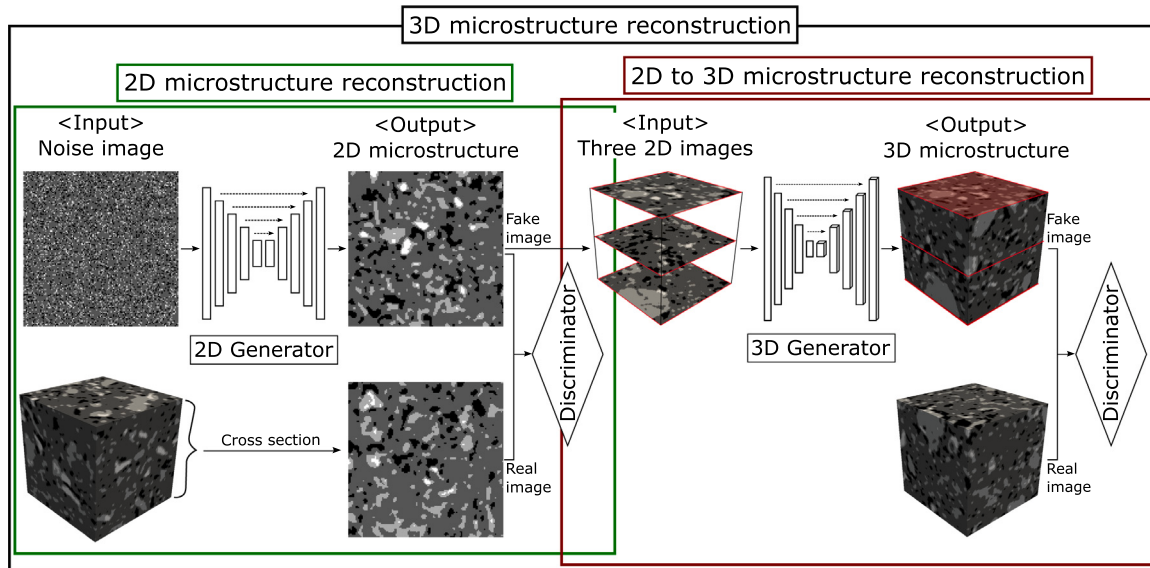


Fig. 6. Modified training network of CycleGAN for reconstructing 3D cement paste microstructure. (Note: The CycleGAN for 3D microstructure reconstruction consists of two processes: the 2D microstructure reconstruction process (green box) and the 2D to 3D microstructure reconstruction process (red box). Each process is equipped with one generator and one discriminator.) (For interpretation of the references to color in this figure legend, the reader is referred to the web version of this article.)

target and reconstructed microstructures. When the validity of the GAN model is tested, the reconstructed images are generally investigated using indices such as the Frechet Inception Distance (FID) [63], which can check the diverse characteristics of the images. However, the reconstruction in this study primarily aimed to obtain microstructures

that yield similar mechanical properties and microstructural characteristics. Thus, microstructural characteristics, such as porosity and phase continuity, were used for the test, and the microstructural characteristics and evaluated material properties of the target and reconstructed microstructures were compared to confirm the validity of the proposed

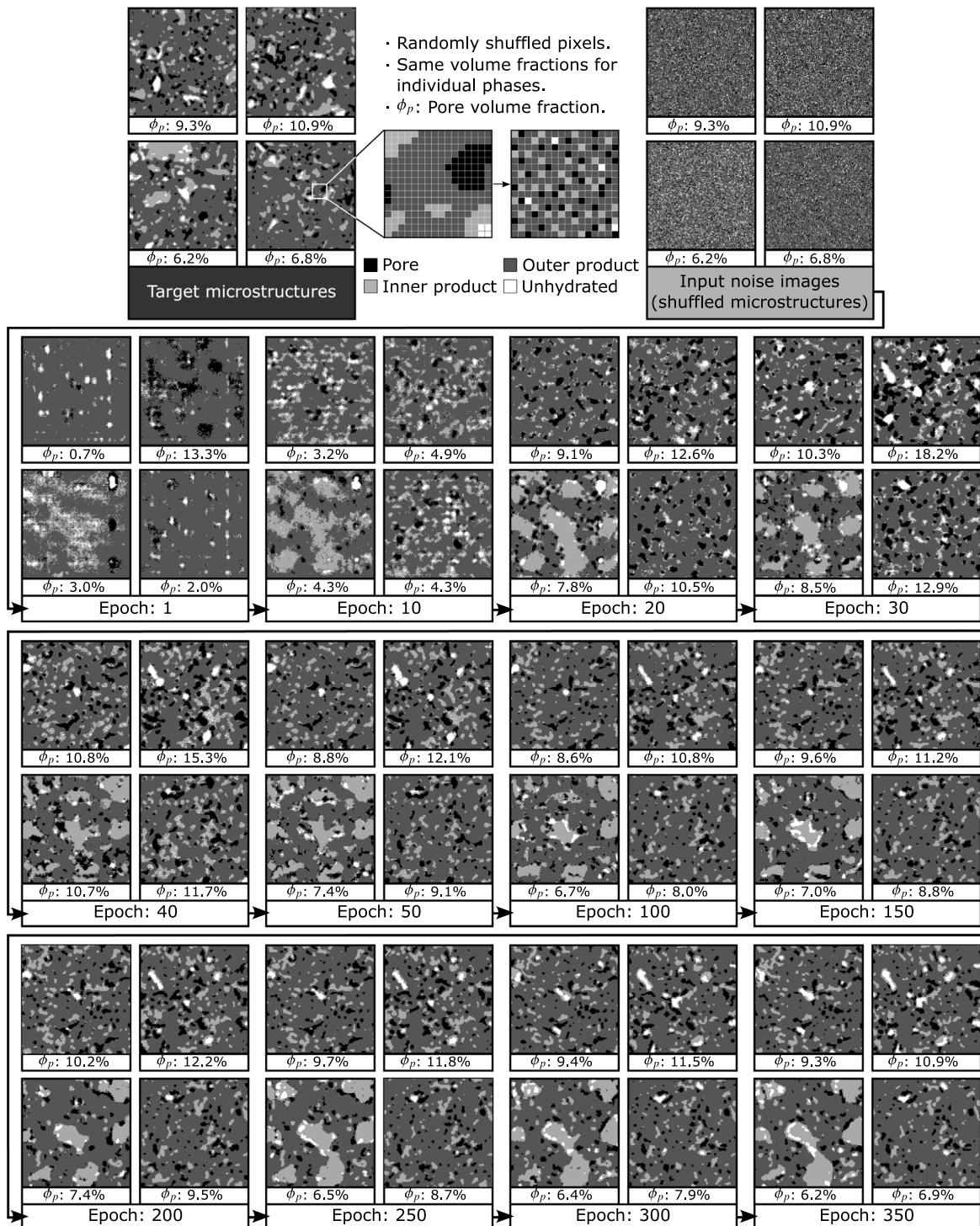


Fig. 7. Reconstructed four-phase microstructures after specific epochs as training progresses. (Note: Four samples are shown for each epoch, one complete pass of the training dataset through the algorithm. The volume fraction of individual phases is the same in the shuffled microstructure.)

reconstruction method. The microstructure generation/reconstruction algorithm was tested on 20 3D real microstructures from micro-CT. Although the number of test samples used in this study could be insufficient for checking the validity of the method using FID, the indices from microstructural characteristics (phase volume fraction and phase continuity) used to test the model were found to be effective and efficient even with a relatively small number of test samples.

The four phases were mapped to the pixel/voxel values of 0, 0.66, 1.33, and 2.0, which represent the pore, outer product, inner product,

and unhydrated phases, respectively. The sequence is the same as the grayscale or LAC values from the micro-CT images, which are generally proportional to the material/phase densities. When the reconstruction process yielded a pixel/voxel value between the phase values, the value was changed to the nearest phase value. The selection of mapped values for phases can be tuned further, including the non-equal-distance phase pixel values; however, this is deferred to a future study. The performance of the algorithms for 2D and 3D microstructure reconstruction is described next.

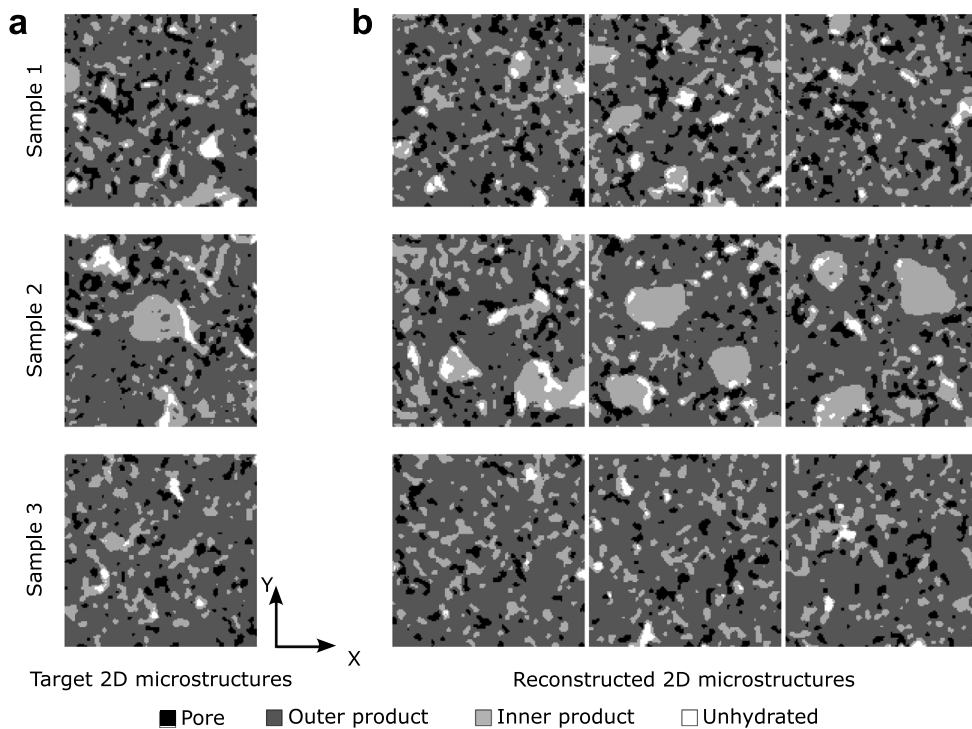


Fig. 8. Examples of reconstructed 2D microstructures. (a) Target microstructures, (b) Reconstructed microstructures. (Sectional images are used for 2D to 3D reconstruction.)

3.2.2. 2D microstructure reconstruction

Once the network is trained and tested, it is ready for microstructure reconstruction. In reconstructing the 2D microstructure, a target microstructure is selected, and volume fractions of the four phases are obtained. A randomly distributed pixel-based (noise) four-phase microstructure image is generated using the volume fractions of the target image and is fed into the trained network for 2D microstructure reconstruction.

The reconstructed microstructures during the training process from the 2D generator are illustrated in Fig. 7. The initial generator produces images with noise. Nevertheless, as the training progresses, the features notably transform and gradually acquire the microstructure characteristics of cement paste. After 350 epochs (the number of complete passes of the training dataset through the algorithm), the reconstructed microstructures did not exhibit noise and rather exhibited similar microstructural features to those of the target microstructure, as confirmed by the indices phase volume fraction and phase continuity. When the training was continued beyond 350 epochs, the reconstructed microstructural features did not improve, and the differences increased owing to overfitting. Because the trained network after 350 epochs exhibited superior performance for reconstructing microstructures for the test data, this network was used for reconstruction. This finding was consistent with the training of the 2D to 3D microstructure reconstruction network described in the next section.

The reconstructed 2D microstructures for 350 epochs are showcased alongside their target counterparts in Fig. 8. In Fig. 8a, there are three target microstructures, labeled samples 1, 2, and 3, each representing different phase cluster sizes. Three microstructures are reconstructed for each sample, shown in Fig. 8b as examples. Notably, the three microstructures reconstructed for one target sample share similar microstructural features, while noticeable differences are visible between the microstructures reconstructed for different target samples. In particular, sample 2 shows a larger cluster of inner products (light gray) in Fig. 8, a characteristic faithfully reproduced in the reconstructed microstructures. Compared with the target microstructures, the pore volume fraction (ϕ_p) differences were within 2%, and the pore and outer product phase continuity (ℓ_L) values were within 5% of those

from the target images for the 500 tested 2D microstructures. Examples of the lineal-path (L) functions of a target and a reconstructed specimen (upper left corner specimens in Fig. 8) are presented in Fig. 9. The lineal-path functions of the 2D microstructure are identified along the x- and y-axis directions, respectively. The results are similar between the target and reconstructed microstructures, which is also true for all other test specimens.

3.2.3. 2D to 3D microstructure reconstruction

A 3D cement paste microstructure is reconstructed from the 2D images (Fig. 6). Three 2D microstructures, generated from random input noise images with the same target phase volume fractions, are provided as the top, middle, and bottom sections for reconstructing the 3D microstructure. When a 3D microstructure is reconstructed, the volume fractions of the pore and outer product phase volume fractions are evaluated. When the volume fraction differences between the target and the reconstructed microstructures are more than 10%, the microstructure is discarded, and the reconstruction process is repeated until the differences are within 10%. The acceptance rate depends on the microstructural characteristics. When the porosity of the target microstructure was similar to that of the samples used for training, the reconstructed microstructures were accepted within 10 attempts. The same behavior was observed in the case of the reconstructed microstructures presented in this manuscript. If the target phase volume fractions are far apart from those of the training microstructures, the acceptance rate of the reconstructed microstructures becomes slow, and the differences in the microstructural features increase. Training with more data possessing a wide range of microstructural features is required to generalize the reconstruction approach, which is deferred to future studies. Examples of reconstructed 3D microstructures are presented with the 3D target cement paste microstructures in Fig. 10. Because the 3D microstructures are reconstructed based on samples 1, 2, and 3 in Fig. 8, the microstructural features observed in the 2D microstructure of samples in Fig. 8 can be observed in the 3D microstructure in Fig. 10. One virtual microstructure was reconstructed from a real microstructure obtained from micro-CT was used for the analysis, resulting in a total of 20 3D virtual microstructures.

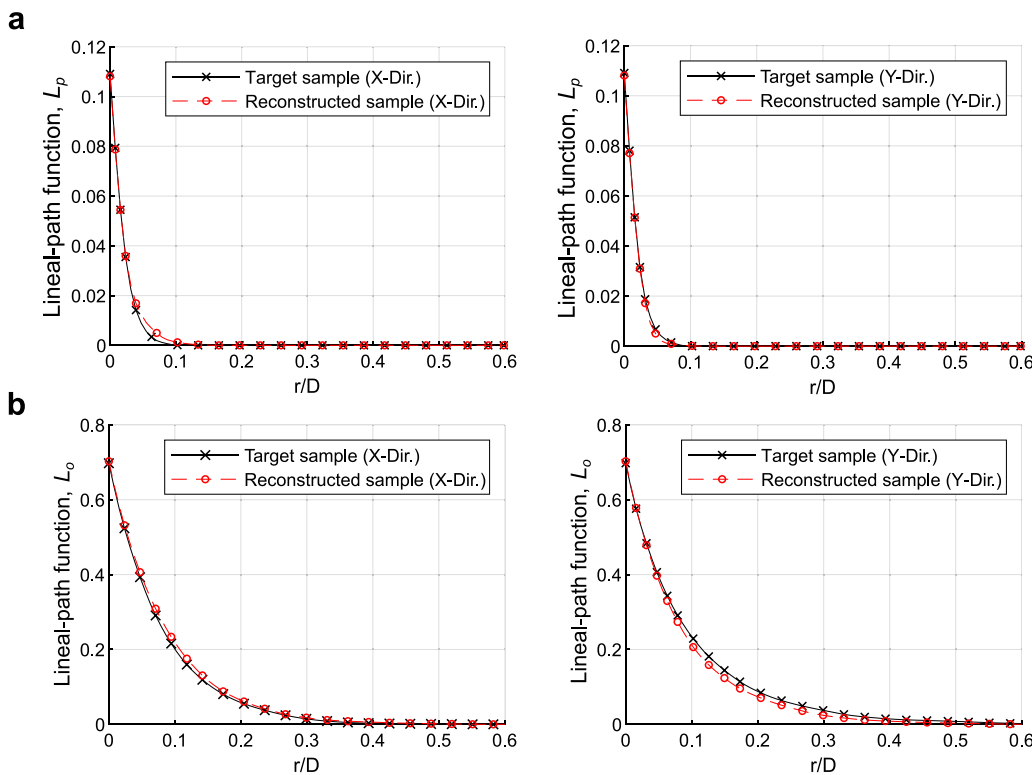


Fig. 9. Lineal-path function for 2D microstructures. (a) Pore phase, (b) Outer product phase. (r : line length, D : sample width)

The differences in the pore and outer product phase volume fractions (ϕ) were within 5%, and those in phase continuity (ℓ_L) were within 7%. The lineal-path functions (L) for the 3D target and reconstructed microstructures are presented in Fig. 11. The lineal-path functions, L_p and L_o , curve for the target microstructure and the reconstructed microstructure also align well for the 3D cases as in 2D. The distributions of porosity (ϕ_p) and outer product phase continuity (ℓ_{L_o}) are presented for all the target and reconstructed specimens (20 each) in Fig. 12. Distributions of volume fractions and phase continuity for other phases were similar. The mean values and standard deviations of ϕ_p and ℓ_{L_o} between the target and reconstructed microstructures are comparable, which confirms that the target and reconstructed specimens share the same statistical microstructural characteristics.

4. Mechanical property evaluation

Using the reconstructed/virtual microstructures and target/original microstructures, mechanical properties (stiffness and tensile strength) were simulated and compared. The simulation procedure is presented first, and evaluated properties from the target and reconstructed microstructures are presented and analyzed.

4.1. Simulation procedure

The mechanical properties of the target and reconstructed microstructures were evaluated using the phase-field fracture model. The input parameters were selected following the procedure presented in Ref. [20] and were briefly described in Section 2.

From the nanoindentation results and micro-CT measurements, the correlation between Young's modulus (E_s) and normalized LAC ($\bar{\chi}_s$) for solid phases was determined as

$$E_s = 69.2 \times \bar{\chi}_s + 1.22 \text{ GPa.} \quad (2)$$

Table 1
Phase characteristics and modeling parameters.

Parameter ^a	Phase			
	Pore	Outer product	Inner product	Unhydrated
ϕ_{target} [%]	9.3	70.3	18.2	2.3
$\phi_{\text{reconstructed}}$ [%]	9.3	69.7	18.3	2.7
$\bar{\chi}_s$ [-]	-	0.143	0.410	1.077
E_s [GPa]	-	11.1	29.6	75.8
σ_s [MPa]	-	31.6	136.3	556.8

^a ϕ is volume fraction; $\bar{\chi}_s$, E_s , and σ_s are normalized LAC, Young's modulus, and tensile strength for solid phase, respectively.

Data pairs of Young's modulus (E_s) and hardness (H_s) for solid phases from the nanoindentation test were approximated using a power law (Fig. 2),

$$H_s = 0.005178 E_s^{1.495} \text{ GPa.} \quad (3)$$

The hardness value is transformed to the tensile strength for a solid phase (σ_s) as

$$\sigma_s = H_s / \xi. \quad (4)$$

Here, ξ is the conversion factor, which depends on materials and varies over a wide range of magnitudes [17]. A ξ value of 12 was reported to be reasonable for cement paste on a similar length scale [17,19], so ξ was set to 12 for the simulations. For each target microstructure, the mean normalized LAC value for the individual solid phase ($\bar{\chi}_s$) is determined, and the input modeling parameters are calculated from Eqs. (2)–(4). Then, the same material modeling parameter values from the target microstructures are assigned to the corresponding reconstructed microstructure. As an example, the phase characteristics and input material modeling parameters for the microstructure at the upper left corner in Fig. 10 are presented in Table 1 [21].

Direct tension was applied to the microstructure as shown in Fig. 13a. The displacement was applied at the top surface while

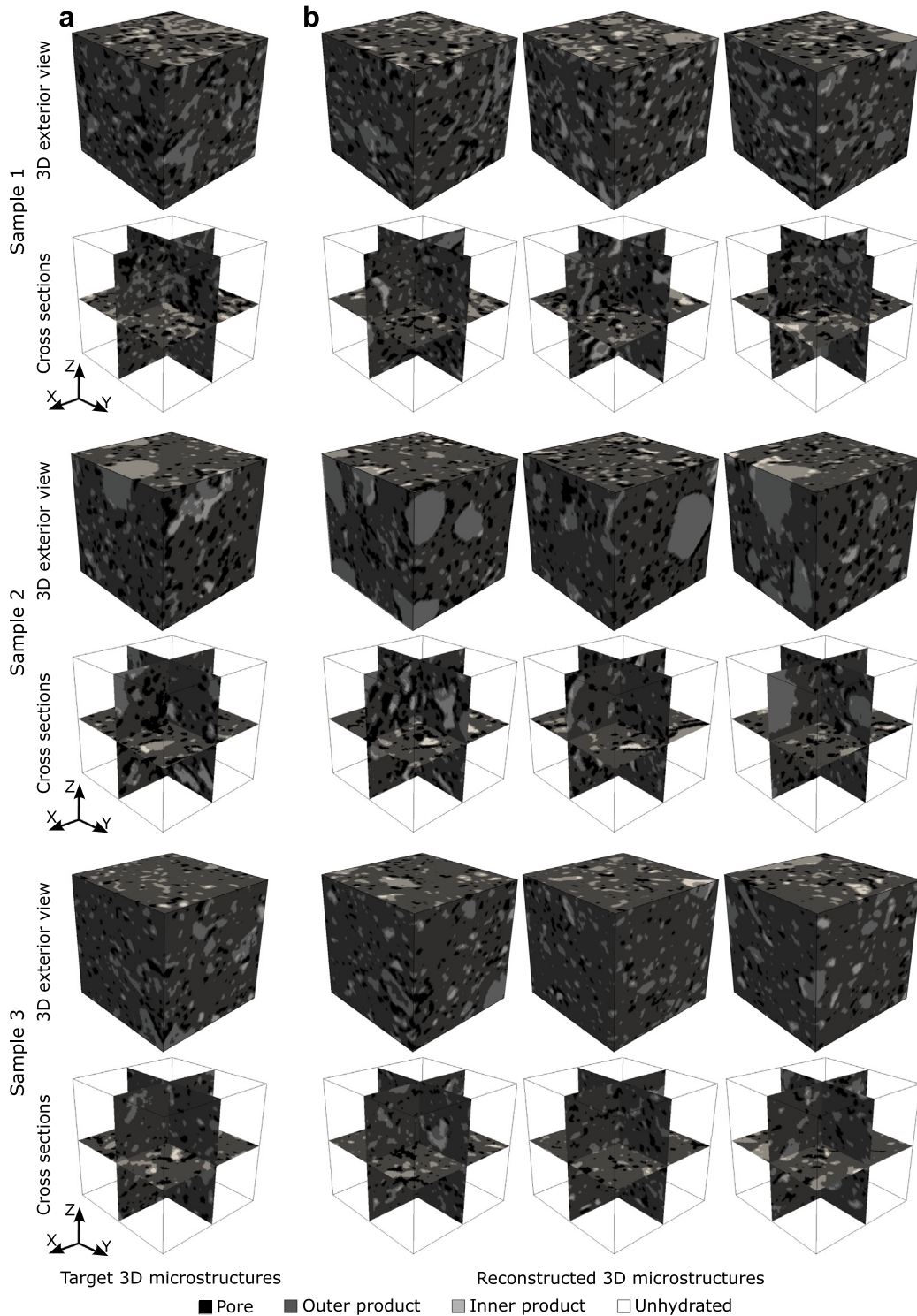


Fig. 10. Examples of reconstructed 3D microstructures. (a) Target microstructures, (b) Reconstructed microstructures.

the bottom was fixed, and the side surfaces were traction-free. The simulations continued over the peak, where multiple crack propagation occurred before the numerical stability was lost. The multiple crack patterns after the peak load and the stress vs. strain curve are shown in Fig. 13b and c, respectively. The simulation time for a model was approximately 7 h using 40 cores of CPUs (Intel Xeon Gold 6148).

4.2. Analysis results

The direct tension simulations were conducted for all the target and reconstructed microstructures. The macroscale stress vs. strain responses of the microstructures are presented in Fig. 14. All 20 specimen responses for each target and reconstructed microstructures are shaded,

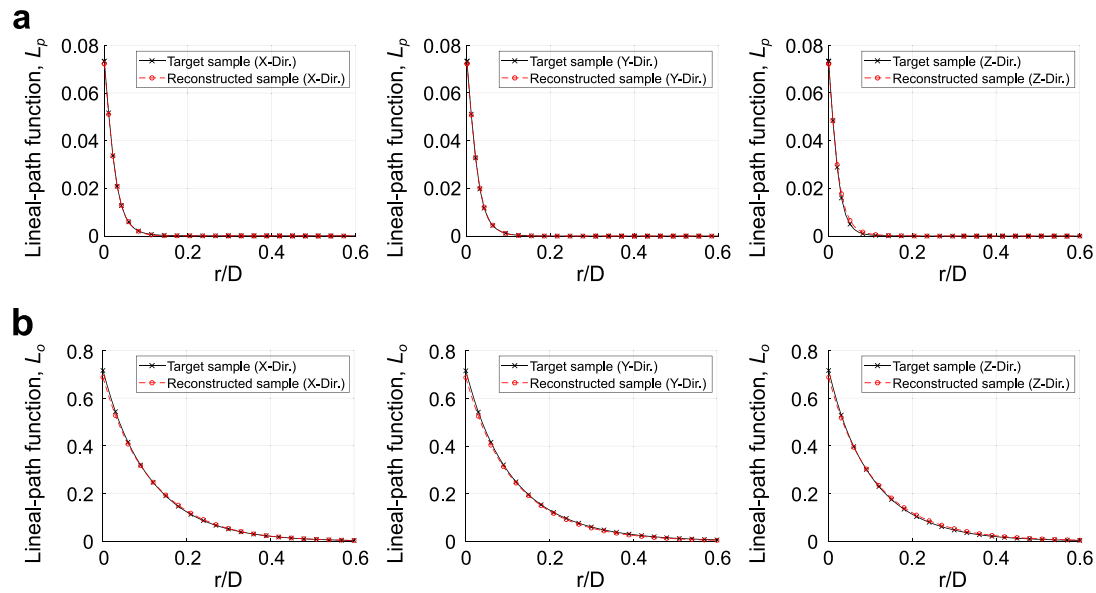


Fig. 11. Lineal-path function for 3D microstructures. (a) Pore phase, (b) Outer product phase. (r : line length, D : sample width)

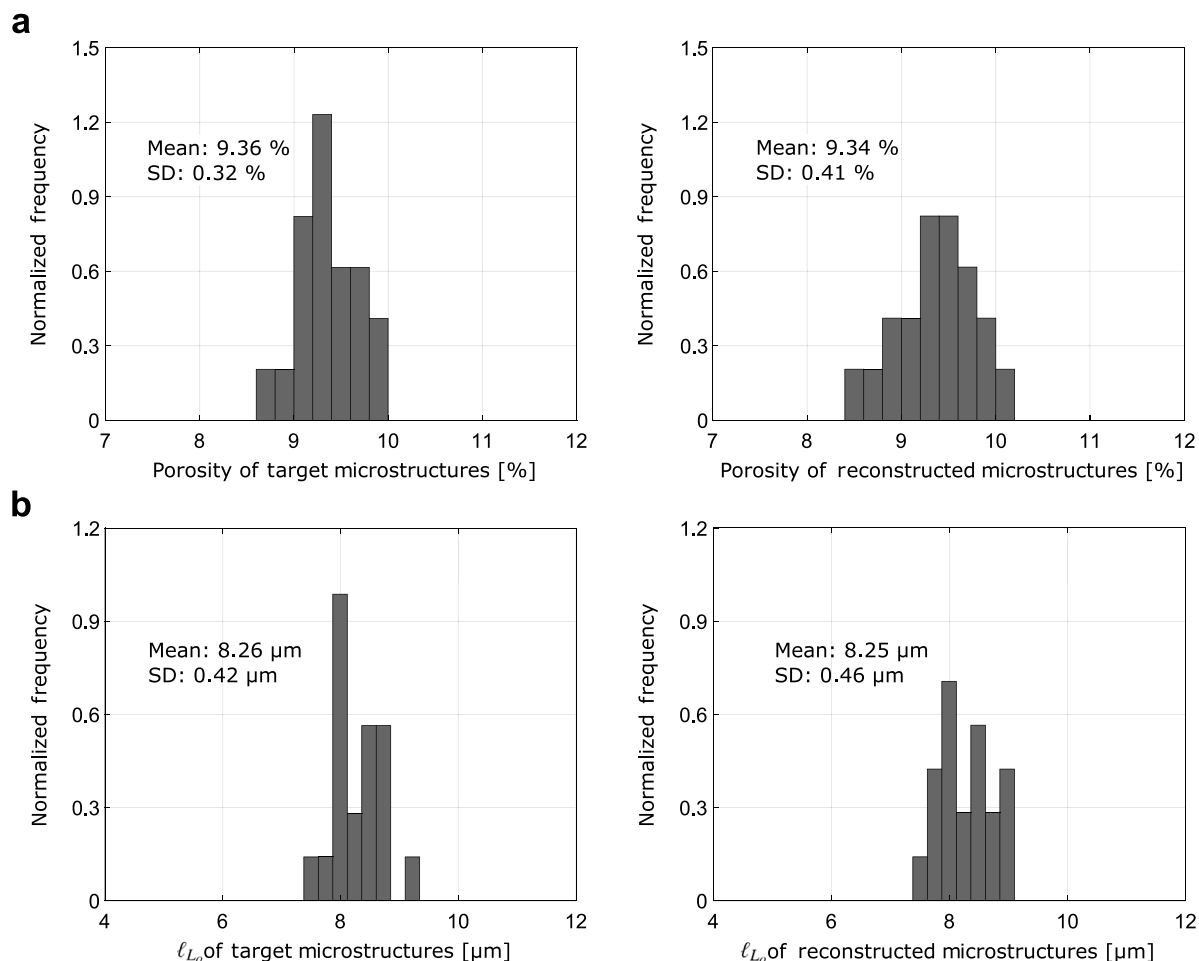


Fig. 12. Distributions of microstructural characteristics. (a) Porosity (ϕ_p), (b) Outer product phase continuity (ℓ_{L_o}).

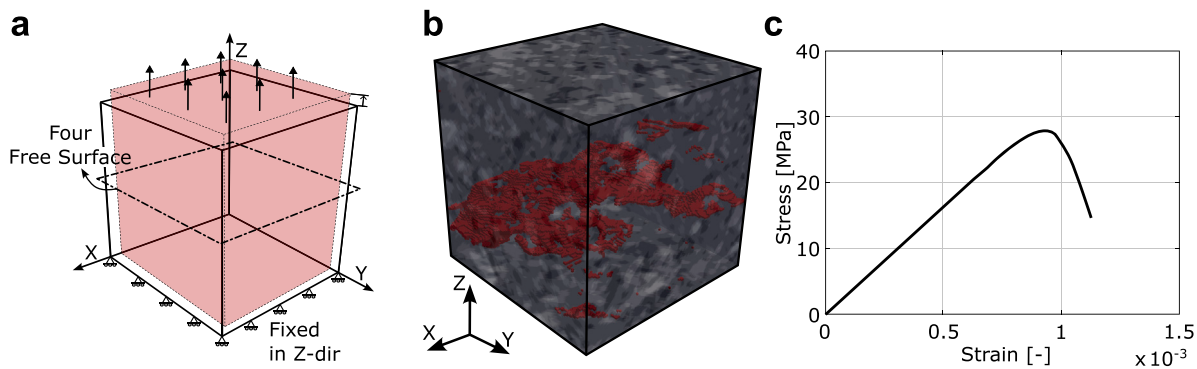


Fig. 13. Simulation setup and responses. (a) Boundary conditions, (b) Crack pattern, (c) Stress vs. strain response.

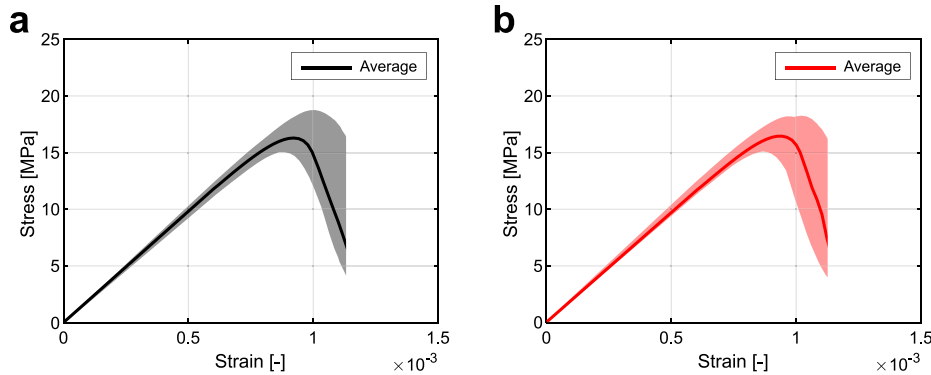


Fig. 14. Stress vs. strain responses of target and reconstructed microstructures. (a) Target samples, (b) Reconstructed samples.

and their averages are plotted as a thick line. There are variations, but the response characteristics from both the target and reconstructed microstructures are similar. The spread of responses, including the stiffness and peak strength values, can be considered as the outcome of uncertainties in the microstructures.

Fig. 15 shows the crack patterns after failure for the cement paste microstructures in Fig. 10. Because of the variations in microstructural features, the crack patterns are not identical. However, the crack pattern characteristics exhibit similarities, such as multiple crack formations and crack propagation through the weakest solid phase (outer product). The inner product volume fractions along the cracked surfaces of the specimens shown in Fig. 15 range from 0.2% to 2.3%, with the exception of target sample 3 (8.1%). Thus, the outer product volume fractions on the crack surfaces were generally greater than 97% and the crack volume from the unhydrated phase on the crack surfaces was negligible. Thus, the cracks do not propagate into the stronger phases but rather through the weaker/outer product phase. The cracks propagated around the stronger phases, as observed in previous studies [19–21, 58].

The distributions of stiffness and tensile strength of the target and reconstructed microstructures are presented in Fig. 16. Consistent with the porosity and phase continuity distributions, the stiffness and strength distribution characteristics between the target and reconstructed microstructures are comparable. The average stiffness of the target and reconstructed microstructures differs by less than 0.3%, and the difference in the average strength is less than 4%. The strength has a larger error compared to the stiffness because various crack patterns can occur due to the diverse local microstructural features. However, considering that the standard deviation of the target microstructures is approximately 23% relative to the average, it is reasonable to conclude that the strength of the reconstructed microstructures is also comparable to that of the target microstructures. The evaluated properties of the reconstructed microstructures are statistically identical to the target microstructures.

It is confirmed from the simulation results that reconstructed microstructures using the proposed adapted CycleGAN approach have material properties similar to those of the target microstructures. Further, all the target and reconstructed microstructures were statistically equivalent [10], which indicates that the material characteristics and properties can be considered the same within tolerance due to the uncertainties inherent to materials with complex microstructures such as cement paste. The reconstructed samples can be treated identically to the target/original microstructures. In this study, only one microstructure was reconstructed from a target microstructure, but this method can be used to reconstruct as many microstructures as needed. Therefore, the number of real experiments can be reduced to obtain microstructures and to evaluate material properties by supplementing real experiments with virtual experiments. This will reduce the time and effort for material property evaluation, accelerating the development of new materials and increasing the reliability of the performance evaluation of existing materials.

5. Summary and discussions

Evaluating material properties from real experiments, including cementitious materials, requires considerable effort to develop new materials and to evaluate the properties of existing materials. Therefore, methods for supplementing time-consuming real experiments with virtual experiments have been investigated. However, the reconstruction of realistic microstructures for virtual experiments is a challenging because of the complexity of microstructural features of cementitious materials. In this study, an artificial-intelligence GAN-based approach was investigated for complex microstructure reconstruction, including vanilla GAN [1] and SliceGAN models [27]. Such models were unable to reconstruct four-phase cement paste microstructures suitable for property evaluation through simulations; therefore, the CycleGAN model [2] was extended to propose a reconstruction approach for

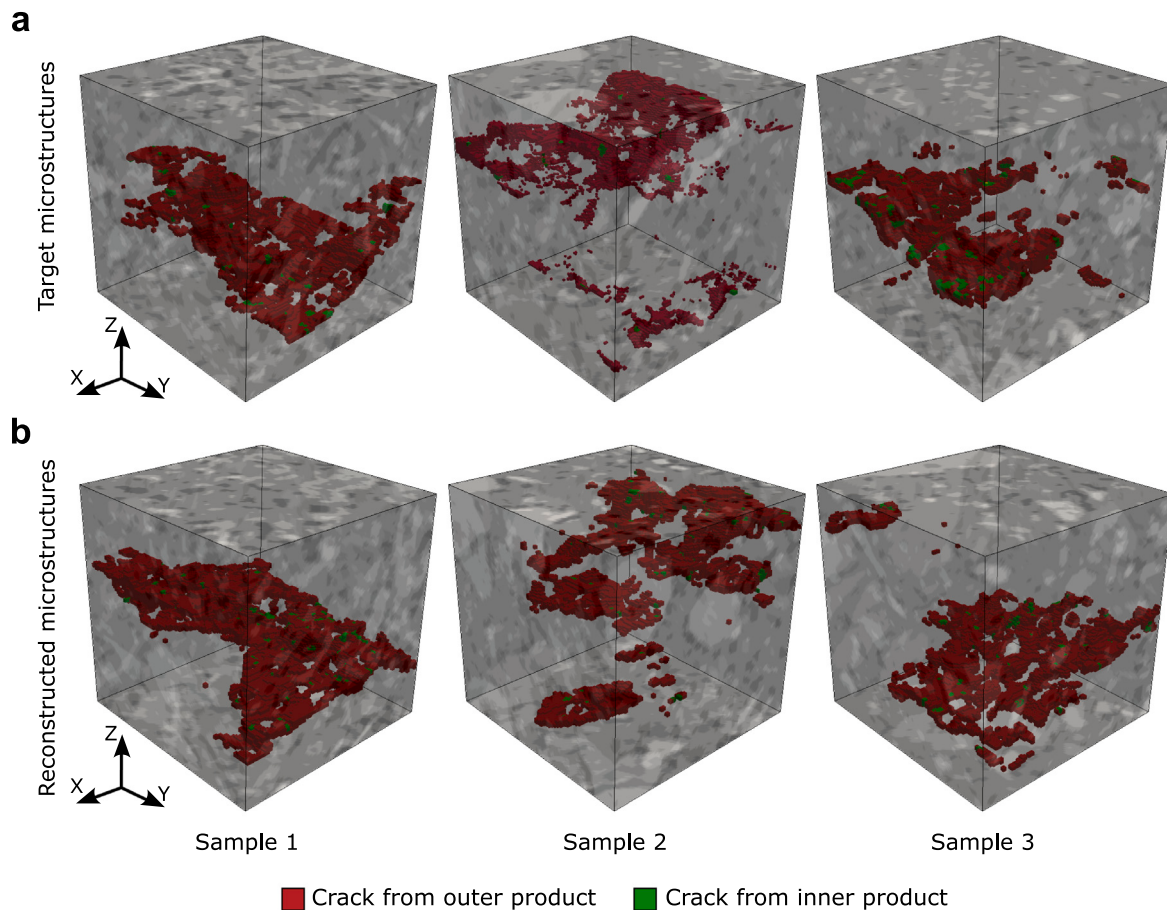


Fig. 15. Examples of crack patterns. (a) Target microstructures, (b) Reconstructed microstructures. (Note: The crack volume from the unhydrated phase is negligible.)

virtual multi-phase cement paste microstructures based on real microstructures obtained from micro-CT measurements. The actual and reconstructed microstructures from the proposed approach shared similar microstructural characteristics, and the evaluated properties were comparable, confirming the validity of the proposed framework. However, the 3D microstructure reconstruction of multi-phase random heterogeneous materials from 2D microstructural images using scanning electron microscopy or transmission electron microscopy is expected to increase the efficiency of the virtual material testing framework. These efforts are planned for future studies.

This study aimed to validate a mechanical property evaluation framework using reconstructed multi-phase cement-paste microstructures. The next step is to calibrate and validate the simulation framework based on the mechanical properties of real experiments. Subsequently, using the data pool from the calibrated analysis framework with deep-learning-generated virtual microstructures, data-driven analysis can be conducted to further confirm the applicability of the framework.

The proposed framework was validated using cement paste specimens with a cement/water ratio of 0.4 after 28 days of hydration. Further confirmation of the robustness of the proposed framework requires additional studies using different cement/water ratios and degrees of hydration. Microstructure reconstruction of cement paste under different conditions can be performed by training the proposed GAN model with the corresponding microstructures. In addition, the proposed reconstruction framework uses a fixed-sized image input and produces the same output microstructures. To produce larger images with more pixels/voxels, the network must be modified, followed by training. However, data preparation and possible model calibration for different conditions require considerable effort. Therefore, these

tasks are deferred to future studies. After validating the robustness of the framework, it should be extended to reconstruct cement paste microstructures with arbitrary microstructural features. This will help establish a correlation between the microstructural characteristics and material properties, resulting in an efficient and effective microstructural design that satisfies the performance requirements through the accurate evaluation of material properties.

The applicability of the framework ranges from experimental confirmation to the statistical data analysis of the evaluated properties. As an example of a statistical and probabilistic application, material property distribution can be identified using the Bayesian approach [64]. The properties evaluated using real experiments are generally expensive. Owing to the uncertainties in microstructural features of cement paste, many microstructures are required to increase reliability. However, statistically equivalent virtual microstructures reconstructed from existing information can reduce the cost and effort required to obtain cement paste microstructures from micro-CT measurements and to evaluate their properties. After conducting a minimum number of real experiments (e.g., 10), simulations can be conducted to obtain additional property data from virtual specimens reconstructed using the proposed framework. The property distributions are then updated using the simulated results, until adequate properties are obtained. These studies require significant efforts and will be considered in the future.

6. Conclusions

This study proposed a method for reconstructing 3D multi-phase cement paste microstructure using artificial intelligence. Based on the CycleGAN algorithm, networks were modified to accommodate the requirements and constraints for the reconstruction process. A two-step process is proposed for efficient and effective reconstruction, in

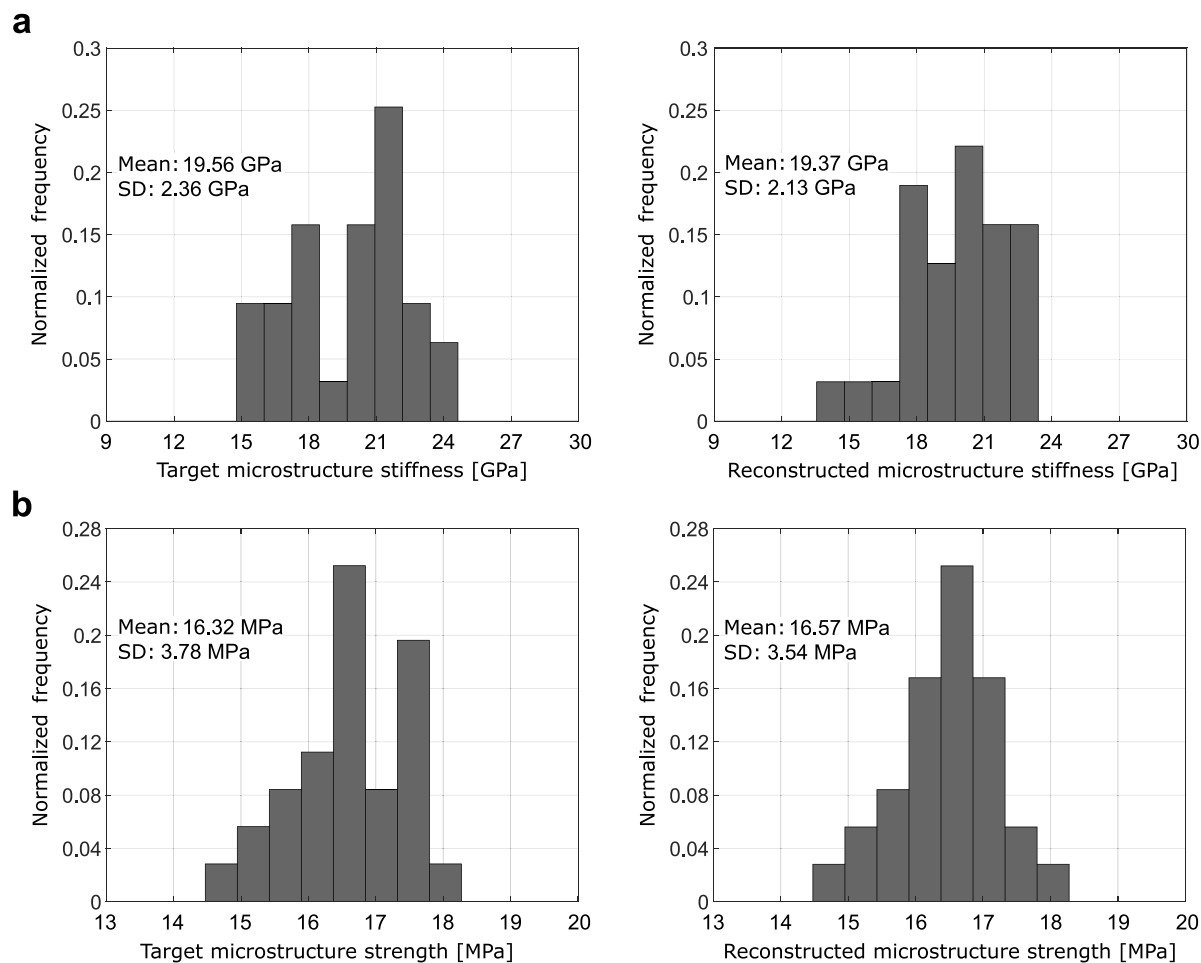


Fig. 16. Property distribution. (a) Stiffness, (b) Strength.

which three 2D sections (top, middle, bottom) of microstructures are reconstructed first, followed by 3D microstructure reconstruction, filling the gap between the sections. By comparing the microstructural characteristics and properties between the target and reconstructed multi-phase cement paste microstructures, the following conclusions are drawn:

- The microstructures reconstructed by the proposed artificial intelligence based method could reproduce the multi-phase cement paste target microstructures from micro-CT and had similar microstructural characteristics, such as volume fractions and phase continuities.
- The mechanical properties (stiffness and tensile strength) of the target and reconstructed cement paste microstructures evaluated using the phase-field fracture model confirmed that the adapted CycleGAN approach can generate the statically equivalent microstructures within uncertainties inherent to the materials.
- Compared with conventional reconstruction approaches, the artificial intelligence based reconstruction method rendered the virtual generation of multi-phase materials with complex microstructures. As the analysis framework is developed further, the framework using the reconstructed microstructures should help reduce the time and effort in conducting real experiments for property evaluation of cementitious materials.

CRediT authorship contribution statement

Sung-Wook Hong: Writing – review & editing, Visualization, Validation, Methodology, Formal analysis, Data curation. **Se-Yun Kim:**

Writing – review & editing, Visualization, Validation, Conceptualization. **Kyoungsoo Park:** Writing – review & editing, Validation, Conceptualization. **Kenjiro Terada:** Validation, Conceptualization. **Hoonhee Lee:** Validation, Resources. **Tong-Seok Han:** Writing – review & editing, Writing – original draft, Validation, Supervision, Methodology, Conceptualization.

Declaration of competing interest

The authors declare that they have no known competing financial interests or personal relationships that could have appeared to influence the work reported in this paper.

Data availability

Data will be made available on request.

Acknowledgments

This study was supported by the National Research Foundation of Korea (NRF-2022R1A4A1033925, RS-2022-00144250, and RS-2024-00352182). This research was also supported by the Technology Innovation Program (RS-2023-00264747, Development of manufacturing technology for blended cement that replaces 15% or more of clinker with calcined clay) funded by the Ministry of Trade, Industry and Energy (MOTIE, Korea). This work was supported by International Joint Research Grant by Yonsei Graduate School, South Korea. The micro-CT images were obtained using a synchrotron operated by the Pohang Accelerator Laboratory (PAL) in the Republic of Korea.

Table A.1
Descriptions of layers and blocks.

	Term ^a	Description
Layer	Conv2D	Extracts features from the 2D-input data in a convolutional neural network (CNN) through downsampling.
	ReLU	Provides nonlinearity to the neural network (activation function) [65].
	MaxPool2D	Extracts the maximum value within a predetermined region to summarize the information of a 2D feature map.
	Flatten	Flattens data into an array (1D vector).
	Dense	Connects all neurons from the previous layer to all neurons in the next layer.
	Dropout	Disables the operation of randomly selected neurons during the learning process to prevent overfitting.
	Reshape	Changes the shape of the data array.
	Conv3D	Extracts features from 3D-input data in a CNN through downsampling.
	Conv3DTranspose	Extracts features from 3D-input data in a CNN through upsampling.
Block	Concat	Connects two sets of data with the same dimensionality to preserve the gradients that diminish as they go backward.
	Conv2D block	Conv2D - ReLU - Conv2D - ReLU - MaxPool2D
	Conv3D block	Conv3D - ReLU - Conv3D - ReLU - Conv3D
	FC block	Dense - Dropout - ReLU

^a Layer name is expressed as the term provided by TensorFlow [59].

Appendix A. Algorithm of CycleGAN

A framework, Generative adversarial network (GAN) [1], is for estimating generative models using the adversarial process. Here, only a brief summary of GAN is presented. The framework comprises two models: $G(z)$ and $D(x)$. $G(z)$ is a generator for reconstructing the data (microstructure in this study) x from a noise variable z , i.e., a mapping $x = G(z)$. $D(x)$, a discriminator, is the probability of sampling data x from the original data set, but not from the reconstructed data. In other words, G generates or reconstructs data with characteristics similar to those of the original samples, and D estimates the probability that the data is from the original samples. D is trained to maximize the probability of identifying the correct source for training data and samples from G . At the same time, G is trained to minimize $\log(1 - D(G(z)))$. Then, the process becomes the optimization problem of the loss or objective function $\mathcal{L}(G, D)$:

$$\min_G \max_D \mathcal{L}(G, D) = \mathbb{E}_{x \sim p_{\text{data}}(x)} [\log D(x)] + \mathbb{E}_{z \sim p_z(z)} [\log(1 - D(G(z)))] , \quad (\text{A.1})$$

where the first term is the expected value of $\log D(x)$ when x is sampled from distribution of data x , $p_{\text{data}}(x)$, and the second term is the expected value of $\log(1 - D(G(z)))$. Two models are trained through an adversarial process by the interactions between the two models, through which the characteristics of the generated data sets become similar to those of the original samples.

Enhanced from general GAN, cycle-consistent generative adversarial networks (CycleGAN) [2] was proposed to reconstruct images more accurately and efficiently. In CycleGAN, the log-likelihood objective from general GAN, Eq. (A.1), is substituted by a least square loss [3] for more stability during training and generation of higher quality results. Also, cycle consistency loss terms are added to improve the image quality by confirming that generated images can inversely generate target images [4]. The algorithm of CycleGAN finds the solution of loss or objective function:

$$\begin{aligned} \min_{G,F} \max_{D_X,D_Y} \mathcal{L}(G, F, D_X, D_Y) &= \mathcal{L}_{\text{LSGAN}}(G, D_Y, X, Y) \\ &+ \mathcal{L}_{\text{LSGAN}}(F, D_X, Y, X) + \lambda \mathcal{L}_{\text{cyc}}(G, F). \end{aligned} \quad (\text{A.2})$$

Here, $G : X \rightarrow Y$ is the generator function that maps the domain X to Y , and D_Y is its discriminator as in the general GAN. $F : Y \rightarrow X$ is the inverse mapping function and D_X is its discriminator. On the right-hand side, the first two terms represent the least square form of loss functions replacing the log form in general GAN, and, for example, the first term takes the form,

$$\begin{aligned} \mathcal{L}_{\text{LSGAN}}(G, D_Y, X, Y) &= \mathbb{E}_{y \sim p_{\text{data}}(y)} [(D_Y(y) - 1)^2] \\ &+ \mathbb{E}_{x \sim p_{\text{data}}(x)} [(D_Y(G(x)))^2]. \end{aligned} \quad (\text{A.3})$$

The last term in the loss function of CycleGAN (Eq. (A.2)) is to enforce the cyclic consistency with the parameter λ for controlling the relative importance of the term and can be expressed as

$$\mathcal{L}_{\text{cyc}}(G, F) = \mathbb{E}_{x \sim p_{\text{data}}(x)} [\|F(G(x)) - x\|_1] + \mathbb{E}_{y \sim p_{\text{data}}(y)} [\|G(F(y)) - y\|_1], \quad (\text{A.4})$$

where $\|\cdot\|_1$ is the L1 norm.

Appendix B. 3D generator

The details of the proposed 3D generator, which uses three 2D images to reconstruct a 3D microstructure in the adapted CycleGAN, are presented. The 2D generator is generally used to reconstruct the 2D image and is generally used in CycleGAN. However, in this study, we propose a 3D generator designed to reconstruct 3D microstructures using 2D images as an extension of the framework provided by TensorFlow [59]. The basic structure of the 3D generator is the same as the 2D generator used in CycleGAN, using an autoencoder [66] consisting of a convolution (encoder) and a transposed convolution (decoder). The 2D generator uses an encoder to compress a 2D image into a 2D feature map, which results from convolutional operation and contains information on the image features. The 2D feature map is then decoded and reconstructed into a 2D image by a decoder. In contrast to the 2D generator, the 3D generator's decoder process involves using a 3D feature map, which is constructed from the encoded 2D feature map. The encoder and decoder process is shown in Fig. A.1a. Descriptions of all the used layers, as termed in TensorFlow, and the blocks (a set of layers) are shown in Table A.1. The 3D generator is based on an autoencoder structure in CycleGAN. It uses two types of connections (Connections A and B) as in Ref. [5] to convert the different dimensions of feature maps in the encoder and decoder.

Connection A

In the encoding process, three 2D images are used as inputs and converted into a 2D feature map through a 2D convolution block (Conv2D block) consisting of five layers in Fig. A.1a. This 2D feature map is further encoded through additional Conv2D blocks and converted to a 3D feature map connected to the decoder (Connection A). Connection A involves a series of steps: (1) flattening the 2D feature map into a 1D vector; (2) applying a fully connected block (FC block); (3) reshaping this 1D vector into a 3D feature map; and (4) finally performing 3D convolution (Conv3D) and ReLU operations, as illustrated in Fig. A.1b. Through Connection A, the 2D feature map at the last output of the encoder is converted into a 3D feature map, which is then employed in the decoder to reconstruct the 3D microstructure via transposed convolution.

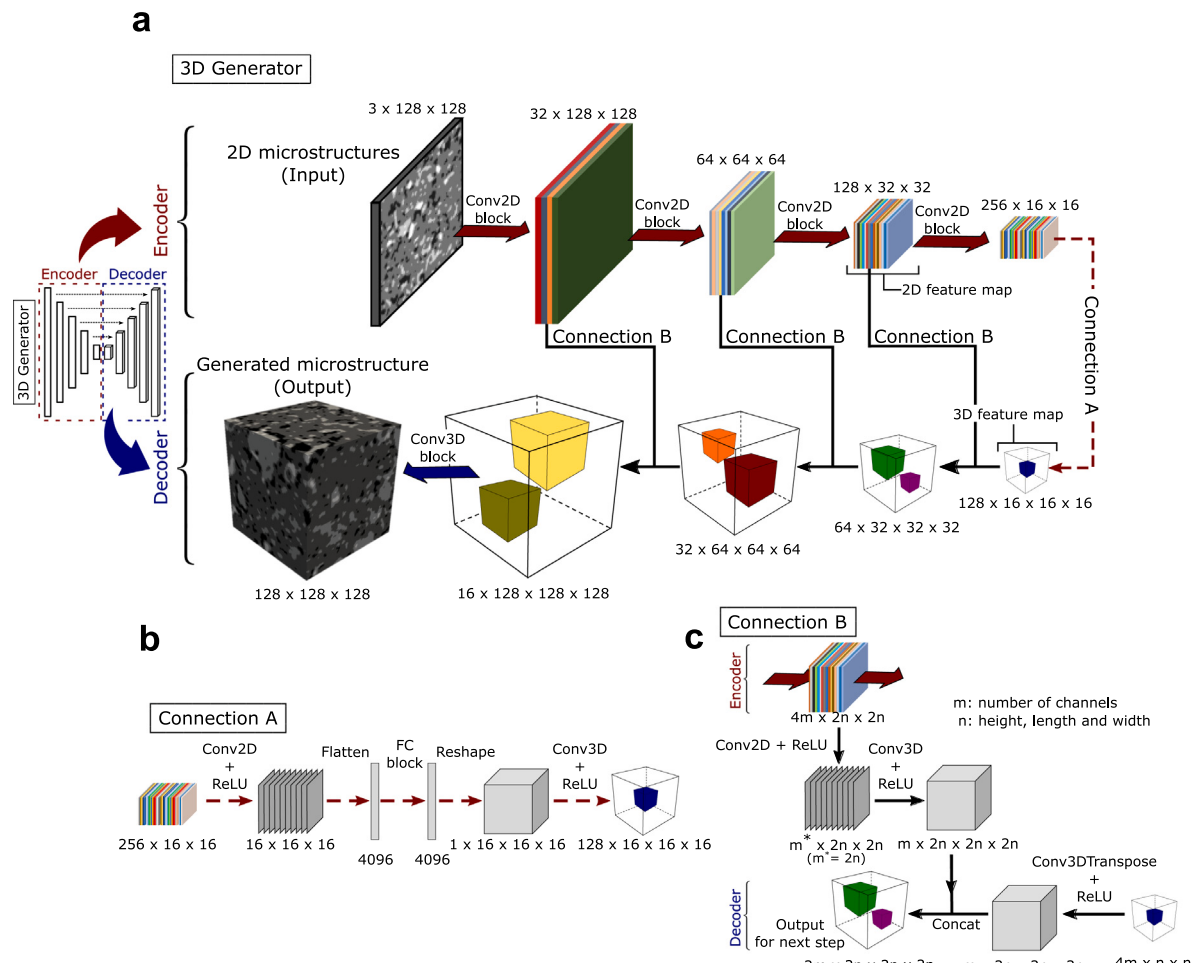


Fig. A.1. 3D Generator model for 2D to 3D microstructure reconstruction incorporating two types of connections between encoder and decoder. (a) A schematic of the 3D generator, (b) Connection A, bridging the encoder and the decoder by a fully connected layer, (c) Connection B adding the information from the 2D to 3D feature maps. (Note: 'n' is the size (height, length, and width) of the 2D or 3D feature, and 'm' is the number of channels, i.e., the quantity of 2D or 3D features. Indicated numbers in feature maps are the actual dimension sizes used in this study.)

Connection B

In CycleGAN, the transposed convolution is the process of decoding the feature map. However, because some information cannot be incorporated into the feature map during the encoding process, additional information is provided during the decoding via the “concatenation” process to obtain better reconstructed microstructures. The concatenation is performed by adding the feature map of the “encoder” to that of the “decoder” to compensate for the information lost during the encoding process. The concatenation is generally the process of combining feature maps in 2D. However, in the proposed 3D generator, the 2D feature map of the encoder and the 3D feature map of the decoder are combined using Connection B shown in Fig. A.1c. Connection B is designed so that the 2D feature map of the encoder has the same dimensions as the 3D feature map. The 2D feature map is converted to the 3D format by a convolution process involving layers using Conv2D and Conv3D. This converted feature map is then concatenated with the 3D feature map, which is passed through the Conv3DTranspose and ReLU layers in the decoder. The 3D feature map generated by the concatenation is used as an input for the next step of the decoder. This process is repeated until the size of the 3D feature map is equal to the size of the 3D microstructure to be reconstructed. Once the 3D feature map becomes the intended size, the 3D convolution block (Conv3D block) comprising five layers converts the feature map into a 3D microstructure.

References

- [1] I. Goodfellow, J. Pouget-Abadie, M. Mirza, B. Xu, D. Warde-Farley, S. Ozair, A. Courville, Y. Bengio, Generative adversarial nets, in: Z. Ghahramani, M. Welling, C. Cortes, N. Lawrence, K. Weinberger (Eds.), Advances in Neural Information Processing Systems, Vol. 27, Curran Associates, Inc., 2014.
- [2] J.-Y. Zhu, T. Park, P. Isola, A.A. Efros, Unpaired image-to-image translation using cycle-consistent adversarial networks, in: Proceedings of the IEEE International Conference on Computer Vision, ICCV, 2017.
- [3] X. Mao, Q. Li, H. Xie, R.Y. Lau, Z. Wang, S. Paul Smolley, Least squares generative adversarial networks, in: Proceedings of the IEEE International Conference on Computer Vision, ICCV, 2017.
- [4] M. Zhang, Pore-scale modelling of relative permeability of cementitious materials using X-ray computed microtomography images, *Cem. Concr. Res.* 95 (2017) 18–29.
- [5] X. Ying, H. Guo, K. Ma, J. Wu, Z. Weng, Y. Zheng, X2CT-GAN: Reconstructing CT from biplanar X-Rays with generative adversarial networks, in: Proceedings of the IEEE/CVF Conference on Computer Vision and Pattern Recognition, CVPR, 2019.
- [6] C.L.Y. Yeong, S. Torquato, Reconstructing random media, *Phys. Rev. E* 57 (1998) 495–506.
- [7] C.L.Y. Yeong, S. Torquato, Reconstructing random media. II. Three-dimensional media from two-dimensional cuts, *Phys. Rev. E* 58 (1998) 224–233.
- [8] D. Cule, S. Torquato, Generating random media from limited microstructural information via stochastic optimization, *J. Appl. Phys.* 86 (1999) 3428–3437.
- [9] C. Manwart, S. Torquato, R. Hilfer, Stochastic reconstruction of sandstones, *Phys. Rev. E* 62 (2000) 893–899.
- [10] S. Torquato, *Random Heterogeneous Materials:Microstructure and Macroscopic Properties*, Springer-Verlag, 2002.
- [11] S.-Y. Chung, T.-S. Han, S.-Y. Kim, T.-H. Lee, Investigation of the permeability of porous concrete reconstructed using probabilistic description methods, *Constr. Build. Mater.* 66 (2014) 760–770.

- [12] S.-Y. Chung, T.-S. Han, S.-Y. Kim, Reconstruction and evaluation of the air permeability of a cement paste specimen with a void distribution gradient using CT images and numerical methods, *Constr. Build. Mater.* 87 (2015) 45–53.
- [13] S.-Y. Kim, J.-S. Kim, J.W. Kang, T.-S. Han, Construction of virtual interfacial transition zone (ITZ) samples of hydrated cement paste using extended stochastic optimization, *Cem. Concr. Compos.* 102 (2019) 84–93.
- [14] J.-S. Kim, S.-Y. Kim, T.-S. Han, Sensitivity and uncertainty estimation of cement paste properties to microstructural characteristics using FOSM method, *Constr. Build. Mater.* 242 (2020) 118159.
- [15] M. Luković, E. Schlangen, G. Ye, Combined experimental and numerical study of fracture behavior of cement paste at the microlevel, *Cem. Concr. Res.* 73 (2015) 123–135.
- [16] H. Zhang, B. Šavija, E. Schlangen, Size effect on splitting strength of hardened cement paste: Experimental and numerical study, *Cem. Concr. Compos.* 94 (2018) 264–276.
- [17] H. Zhang, B. Šavija, M. Luković, E. Schlangen, Experimentally informed micromechanical modelling of cement paste: An approach coupling X-ray computed tomography and statistical nanoindentation, *Composites B* 157 (2019) 109–122.
- [18] H. Zhang, Y. Xu, Y. Gan, Z. Chang, E. Schlangen, B. Šavija, Combined experimental and numerical study of uniaxial compression failure of hardened cement paste at micrometre length scale, *Cem. Concr. Res.* 126 (2019) 105925.
- [19] J.-S. Kim, J.-H. Lim, D. Stephan, K. Park, T.-S. Han, Mechanical behavior comparison of single and multiple phase models for cement paste using micro-CT images and nanoindentation, *Constr. Build. Mater.* 342 (2022) 127938.
- [20] T.-S. Han, D. Eum, S.-Y. Kim, J.-S. Kim, J.-H. Lim, K. Park, D. Stephan, Multi-scale analysis framework for predicting tensile strength of cement paste by combining experiments and simulations, *Cem. Concr. Compos.* 139 (2023) 105006.
- [21] S.-Y. Kim, D. Eum, H. Lee, K. Park, K. Terada, T.-S. Han, Evaluating tensile strength of cement paste using multiscale modeling and *in-situ* splitting tests with micro-CT, *Constr. Build. Mater.* 411 (2024) 134642.
- [22] X. Li, Y. Zhang, H. Zhao, C. Burkhardt, L.C. Brinson, W. Chen, A transfer learning approach for microstructure reconstruction and structure-property predictions, *Sci. Rep.* 8 (2018) 13462.
- [23] R. Bostanabad, Reconstruction of 3D microstructures from 2D images via transfer learning, *Comput. Aided Des.* 128 (2020) 102906.
- [24] P. Seibert, A. Raßloff, K.A. Kalina, J. Gussone, K. Bugelnig, M. Diehl, M. Kästner, Two-stage 2D-to-3D reconstruction of realistic microstructures: Implementation and numerical validation by effective properties, *Comput. Methods Appl. Mech. Engrg.* 412 (2023) 116098.
- [25] J. Fu, D. Xiao, D. Lib, H.R. Thomas, C. Li, Stochastic reconstruction of 3D microstructures from 2D cross-sectional images using machine learning-based characterization, *Comput. Methods Appl. Mech. Engrg.* 390 (2022) 114532.
- [26] J. Feng, Q. Teng, B. Lic, X. He, H. Chen, Y. Li, An end-to-end three-dimensional reconstruction framework of porous media from a single two-dimensional image based on deep learning, *Comput. Methods Appl. Mech. Engrg.* 368 (2020) 113043.
- [27] S. Kench, I. Squires, A. Dahari, S. Cooper, MicroLib: A library of 3D microstructures generated from 2D micrographs using SliceGAN, *Sci. Data* 9 (2022) 645.
- [28] E. Kononov, M. Tashkinov, V. Silberschmidt, Reconstruction of 3D random media from 2D images: Generative adversarial learning approach, *Comput. Aided Des.* 158 (2023) 103498.
- [29] Y. Dong, P. Qiao, CT image-based synthetic mesostructure generation for multiscale fracture analysis of concrete, *Constr. Build. Mater.* 296 (2021) 123582.
- [30] J. Lin, S. Chen, W. Wang, C. Pathirage, L. Li, K. Sagoe-Crentsil, W. Duan, Transregional spatial correlation revealed by deep learning and implications for material characterisation and reconstruction, *Mater. Charact.* 178 (2021) 111268.
- [31] Y. Huang, Z. Xiang, M. Qian, Deep-learning-based porous media microstructure quantitative characterization and reconstruction method, *Phys. Rev. E* 105 (2022) 015308.
- [32] T. Zhang, M. Ni, Q. Guan, D. Li, S. Zhou, Y. Du, Reconstruction of three-dimensional porous media using multi-scale generative adversarial networks, *J. Appl. Geophys.* 213 (2023) 105042.
- [33] J. Guo, C.L.P. Chen, L. Wang, B. Yang, T. Zhang, L. Zhang, Constructing microstructural evolution system for cement hydration from observed data using deep learning, *IEEE Trans. Syst. Man Cybern. Syst.* 53 (7) (2023) 4576–4589.
- [34] D.P. Kingma, M. Welling, Auto-encoding variational Bayes, 2013, arXiv:1312.6114.
- [35] S. Noguchi, J. Inoue, Stochastic characterization and reconstruction of material microstructures for establishment of process-structure-property linkage using the deep generative model, *Phys. Rev. E* 104 (2021) 025302.
- [36] L. Xu, N. Hoffman, Z. Wang, H. Xu, Harnessing structural stochasticity in the computational discovery and design of microstructures, *Mater. Des.* 223 (2022) 111223.
- [37] J. Sohl-Dickstein, E. Weiss, N. Maheswaranathan, S. Ganguli, Deep unsupervised learning using nonequilibrium thermodynamics, in: F. Bach, D. Blei (Eds.), Proceedings of the 32nd International Conference on Machine Learning, in: Proceedings of Machine Learning Research, vol. 37, PMLR, Lille, France, 2015, pp. 2256–2265.
- [38] C. Düreth, P. Seibert, D. Rücker, S. Handford, M. Kästner, M. Gude, Conditional diffusion-based microstructure reconstruction, *Mater. Today Commun.* 35 (2023) 105608.
- [39] K.-H. Lee, H.J. Lim, G.J. Yun, A data-driven framework for designing microstructure of multifunctional composites with deep-learned diffusion-based generative models, *Eng. Appl. Artif. Intell.* 129 (2024) 107590.
- [40] P. Monteiro, G. Geng, D. Marchon, J. Li, P. Alapati, K. Kurtis, M. Qomi, Advances in characterizing and understanding the microstructure of cementitious materials, *Cem. Concr. Res.* 124 (2019) 105806.
- [41] S.-Y. Chung, J.-S. Kim, D. Stephan, T.-S. Han, Overview of the use of micro-computed tomography (micro-CT) to investigate the relation between the material characteristics and properties of cement-based materials, *Constr. Build. Mater.* 229 (2019) 116843.
- [42] S. Brisard, M. Serdar, P. Monteiro, Multiscale X-ray tomography of cementitious materials: A review, *Cem. Concr. Res.* 128 (2020) 105824.
- [43] H. Zhang, Y. Gan, Z. Chang, E. Schlangen, B. Šavija, Microstructure informed micromechanical modelling of hydrated cement paste: Techniques and challenges, *Constr. Build. Mater.* 251 (2020) 118983.
- [44] M. Zhang, A. Jivkov, Micromechanical modelling of deformation and fracture of hydrating cement paste using X-ray computed tomography characterisation, *Composites B* 88 (2016) 64–72.
- [45] J. Huang, K. Krabbenhoft, A. Lyamin, Statistical homogenization of elastic properties of cement paste based on X-ray microtomography images, *Int. J. Solids Struct.* 50 (2013) 699–709.
- [46] M. Hain, P. Wriggers, Numerical homogenization of hardened cement paste, *Comput. Mech.* 42 (2008) 197–212.
- [47] T. Wu, İ. Temizer, P. Wriggers, Computational thermal homogenization of concrete, *Cem. Concr. Compos.* 35 (2013) 59–70.
- [48] T. Nguyen, A. Ghazlan, A. Kashani, S. Bordas, T. Ngo, 3D meso-scale modelling of foamed concrete based on X-ray computed tomography, *Constr. Build. Mater.* 188 (2018) 583–598.
- [49] C. Miehe, M. Hofacker, F. Welschinger, A phase field model for rate-independent crack propagation: Robust algorithmic implementation based on operator splits, *Comput. Methods Appl. Mech. Engrg.* 199 (2010) 2765–2778.
- [50] C. Miehe, L.-M. Schäzel, H. Ulmer, Phase field modeling of fracture in multi-physics problems. Part I: Balance of crack surface and failure criteria for brittle crack propagation in thermo-elastic solids, *Comput. Methods Appl. Mech. Engrg.* 294 (2015) 449–485.
- [51] J.-S. Kim, J. Suh, J. Pae, J. Moon, T.-S. Han, Gradient-based phase segmentation method for characterization of hydrating cement paste microstructures obtained from X-ray micro-CT, *J. Build. Eng.* 46 (2022) 103721.
- [52] J. Němeček, J. Lukeš, J. Němeček, High-speed mechanical mapping of blended cement pastes and its comparison with standard modes of nanoindentation, *Mater. Today Commun.* 23 (2020) 100806.
- [53] B. Cullity, S. Stock, Elements of X-ray Diffraction, Prentice Hall, 2001.
- [54] T.-S. Han, X. Zhang, J.-S. Kim, S.-Y. Chung, J.-H. Lim, C. Linder, Area of linal-path function for describing the pore microstructures of cement paste and their relations to the mechanical properties simulated from μ -CT microstructures, *Cem. Concr. Compos.* 89 (2018) 1–17.
- [55] J.-S. Kim, J. Kim, T.-S. Han, Microstructure characterization of cement paste from micro-CT and correlations with mechanical properties evaluated from virtual and real experiments, *Mater. Charact.* 155 (2019) 109807.
- [56] J.-S. Kim, S.-Y. Chung, D. Stephan, T.-S. Han, Issues on characterization of cement paste microstructures from μ -CT and virtual experiment framework for evaluating mechanical properties, *Constr. Build. Mater.* 202 (2019) 82–102.
- [57] J.-S. Kim, S.-Y. Chung, T.-S. Han, D. Stephan, M. Elrahman, Correlation between microstructural characteristics from micro-CT of foamed concrete and mechanical behaviors evaluated by experiments and simulations, *Cem. Concr. Compos.* 112 (2020) 103657.
- [58] J.-S. Kim, S.-Y. Chung, T.-S. Han, D. Stephan, M. Elrahman, Modeling of multiple phase solid microstructures and prediction of mechanical behaviors of foamed concrete, *Constr. Build. Mater.* 248 (2020) 118637.
- [59] M. Abadi, A. Agarwal, P. Barham, E. Brevdo, Z. Chen, C. Citro, G.S. Corrado, A. Davis, J. Dean, M. Devin, S. Ghemawat, I. Goodfellow, A. Harp, G. Irving, M. Isard, Y. Jia, R. Jozefowicz, L. Kaiser, M. Kudlur, J. Levenberg, D. Mane, R. Monga, S. Moore, D. Murray, C. Olah, M. Schuster, J. Shlens, B. Steiner, I. Sutskever, K. Talwar, P. Tucker, V. Vanhoucke, V. Vasudevan, F. Viegas, O. Vinyals, P. Warden, M. Wattenberg, M. Wicke, Y. Yu, X. Zheng, Tensorflow: Large-scale machine learning on heterogeneous distributed systems, 2015, Software available from tensorflow.org.
- [60] I. Gitman, H. Askes, L. Sluys, Representative volume: existence and size determination, *Eng. Fract. Mech.* 74 (2007) 2514–2534.
- [61] Y. LeCun, B. Boser, J. Denker, D. Henderson, R. Howard, W. Hubbard, L. Jackel, Handwritten digit recognition with a back-propagation network, *Adv. Neural Inf. Process. Syst.* 2 (1989) 396–404.
- [62] P. Isola, J.-Y. Zhu, T. Zhou, A.A. Efros, Image-to-image translation with conditional adversarial networks, in: Proceedings of the IEEE Conference on Computer Vision and Pattern Recognition, 2017, pp. 1125–1134.

- [63] M. Heusel, H. Ramsauer, T. Unterthiner, B. Nessler, S. Hochreiter, GANs trained by a two time-scale update rule converge to a local Nash equilibrium, in: *Advances in Neural Information Processing Systems*, Vol. 30, Curran Associates, Inc., 2017.
- [64] A. Ang, W. Tang, *Probability Concepts in Engineering: Emphasis on Applications to Civil and Environmental Engineering*, second ed., Wiley, 2006.
- [65] V. Nair, G.E. Hinton, Rectified linear units improve restricted boltzmann machines, in: *Proceedings of the 27th International Conference on Machine Learning*, ICML-10, 2010, pp. 807–814.
- [66] J. Masci, U. Meier, D. Cireşan, J. Schmidhuber, Stacked convolutional auto-encoders for hierarchical feature extraction, in: *Artificial Neural Networks and Machine Learning—ICANN 2011: 21st International Conference on Artificial Neural Networks*, Espoo, Finland, Springer, 2011, pp. 52–59.